

GP Bandit-Assisted Two-Stage Sparse Phase Retrieval for Amplitude-Only Near-Field Beam Training

Zijun Wang, Shawn Tsai, Ye Hu, *Member, IEEE*, Rui Zhang, *Member, IEEE*

Abstract—The transition to Extremely Large Antenna Arrays (ELAA) in 6G introduces significant near-field effects, necessitating robust near-field beam training strategies in multi-path environments. Because signal phases are frequently compromised by hardware impairments such as phase noise and frequency offsets, amplitude-only channel recovery is a critical alternative to coherent beam training. However, existing near-field amplitude-based training methods often assume simplistic line-of-sight conditions. Conversely, far-field phase retrieval (PR) methods lack the sensing flexibility required to optimize training efficiency and are fundamentally limited by plane-wave models, making them ill-suited for near-field propagation. We propose a two-stage sparse PR framework for amplitude-only near-field beam training in multipath channels. Stage I performs adaptive support discovery on the standard 2D DFT beamspace by exploiting a physics-guided prior induced by near-field beam patterns. Stage II then refines the channel estimate by restricting sensing and sparse PR to the learned subspace. Numerical results show that the proposed adaptive pipeline consistently outperforms non-adaptive baselines, improving beamforming gain by over 70% at low SNR.

Index Terms—Near-field communications, ELAA, beam training, adaptive phase retrieval, Gaussian-process bandit.

I. INTRODUCTION

THE vision for 6G wireless networks centers on a multi-tier spectrum strategy, leveraging the upper mid-band, millimeter-wave, and Terahertz frequencies to meet the demand for Gbps-scale capacity, sub-millisecond latency, and ubiquitous coverage [1], [2], [3]. While these bands offer vast bandwidth, they also suffer from severe propagation and atmospheric absorption losses. To sustain a viable link budget, 6G base stations will deploy extremely large antenna arrays (ELAA) with hundreds or thousands of elements, providing the high beamforming gain necessary to overcome these path losses [4], [5]. However, the combination of massive physical apertures and short wavelengths pushes the some typical communication distances into the near-field regime [6], [7]. In this regime, the traditional far-field plane-wave assumption is no longer valid. Instead, the channel is characterized by spherical wavefronts, where the array response depends on

both the user’s angular direction and their specific propagation range [8].

This shift has motivated extensive studies on near-field channel modeling, channel estimation and beam management [9], [10], [11], [12]. Under the assumption of phase-coherent measurements, near-field channel acquisition generally falls into two categories: parametric inference and compressive sparse recovery. Within the parametric framework, subspace-based methods leverage the eigenstructure of the sample covariance matrix to distinguish signal and noise subspaces, subsequently identifying path parameters through high-resolution spectrum searches. For instance, [13] utilizes DFT-codebook sweeping to collect complex measurements, employing a MUSIC-type spectrum to isolate dominant angular components, followed by a matched-filter-based range scan for distance refinement. To mitigate the computational intensity of such searches, [14] introduces a reduced-dimension near-field MUSIC formulation, enabling efficient joint angle-range estimation that scales effectively with the massive apertures of ELAAs. Complementing these subspace approaches are likelihood-driven estimation methods, which formulate channel acquisition as a maximum-likelihood estimation (MLE) problem under a spherical-wave model. Building on the polar-domain codebook proposed in [9], a Gaussian MLE approach is used to refine off-grid Uniform Linear Array (ULA) estimates, while [15] extends this refinement to Uniform Planar Arrays (UPA). Beyond parametric fitting, the inherent sparsity of high-frequency channels allows near-field training to be framed as a compressive sensing (CS) problem. Early works in hybrid-beamforming architectures, such as [16], designed training precoders and combiners that utilize Orthogonal Matching Pursuit (OMP) to identify dominant spatial paths. This framework was further generalized in [17] to accommodate various hybrid hardware constraints. Transitioning to the near-field, [18] exploits a polar-domain dictionary to represent the channel’s joint angle-range sparsity, significantly reducing the reporting overhead of beam training compared to exhaustive two-dimensional sweeping under multi-path scenarios.

Despite the efficacy of coherent methods, phase stability is often a fragile assumption in practical transceivers. Residual synchronization errors and hardware impairments, including carrier-frequency offset, phase noise, and frequency drift, introduce unknown, time-varying distortions across training slots, preventing the coherent combination of pilot observations [19]. Consequently, there is a compelling need for non-coherent beam training and channel estimation strategies that rely exclusively on amplitude-only feedback. Un-

Zijun Wang, and Rui Zhang are with the Department of Electrical Engineering, The State University of New York at Buffalo, New York, USA (email: zwang267@buffalo.edu, rzhang45@buffalo.edu). Shawn Tsai is with the CSD, MediaTek Inc. USA, San Diego, CA 92122 USA (e-mail: shawn.tsai@mediatek.com). Ye Hu is with the Industrial and Systems Engineering, and Department of Electrical and Computer Engineering, University of Miami, Florida, USA (email: yehu@miami.edu).

This work was supported in part by the CSD, MediaTek Inc. USA, under Grant 103764, and in part by the National Science Foundation, under Grant ECCS 2512911.

Corresponding author: Rui Zhang.

der amplitude-only acquisition, the most intuitive baseline is codebook sweeping combined with power-based best beam selection. In near-field systems, polar-domain codebooks discretize both angle and range to provide the fine spatial focusing required for spherical-wave propagation [9]. However, exhaustive searching over a two-dimensional angle-range grid incurs prohibitive overhead. To mitigate this, hierarchical and structured codebook designs have been proposed to localize promising spatial regions before performing fine-grained refinement. For instance, [20] utilizes a two-layer polar-domain codebook for low-overhead region searching, while [12] introduces a "slope-intercept" representation to decouple chirp-like parameters, organizing beams into a hierarchical search that reduces inter-codeword correlation. While effective for single-path Line-of-Sight (LoS) scenarios, these sweeping strategies often overlook multi-path environments where multiple spatial components must be resolved.

In multi-path channels, robust beamforming requires recovering both the dominant paths and their associated complex combining coefficients. With amplitude-only measurements, this task evolves into a phaseless inverse problem, where the goal is to recover the channel vector \mathbf{x} from magnitude measurements $y_i = |\langle \mathbf{a}_i, \mathbf{x} \rangle|$ or $y_i^2 = |\langle \mathbf{a}_i, \mathbf{x} \rangle|^2$. Classical Wirtinger Flow (WF) solvers, such as Truncated Wirtinger Flow (TWF) and Truncated Amplitude Flow (TAF), employ spectral initialization followed by gradient-descent updates on intensity-based losses, using truncation rules to enhance robustness against outliers [21], [22]. However, these general solvers do not exploit the structured sparsity inherent in high-frequency wireless channels. While sparse PR variants like Sparse Wirtinger Flow (SWF) and Sparse Phase Retrieval via Truncated Amplitude Flow (SPARTA) [23], [24] incorporate hard-thresholding to pursue sparse supports, they are not tailored for beam training; they typically require a pre-specified sparsity level and rely on non-adaptive sensing matrices, missing the opportunity to reduce sweeping overhead through intelligent, real-time probing. Non-coherent beam training has been studied in far-field wireless systems, which is typically framed as sparse PR or phaseless decoding. Works such as [25] enable the recovery of dominant angular beams from compressive magnitude measurements, while [19] and [26] handle unknown phase offsets and channel tracking through phase-modulated probing. However, these methods are built upon the plane-wave far-field model, where sparsity is defined on an angular dictionary. They fail to account for the near-field spherical-wave effect, where steering depends jointly on angle and range.

Consequently, a significant gap remains: how to achieve low-overhead, non-coherent near-field beam training in multi-path environments? To address this challenge, we propose a Gaussian bandit-assisted sparse phase retrieval framework for amplitude-only near-field beam training. Our approach utilizes a two-stage design. First, the base station performs a coarse, low-overhead support discovery using DFT beams, guided by an adaptive Gaussian Process (GP) bandit policy to prioritize promising directions. Second, the base station executes sparse PR exclusively on the estimated support using a Gaussian-masked DFT sensing matrix. To the best of our knowledge,

this is the first work to perform amplitude-only near-field beam training for multi-path channels with an adaptive, bandit-guided sparse phase retrieval framework.

The main contributions of this work are summarized as follows:

- **DFT beamspace modeling for near-field channels and beam pattern analysis:** We adopt the standard DFT codebook as the beamspace representation to ensure compatibility with far-field systems. To address the inherent near-field spatial mismatch, we provide a rigorous analysis of the DFT beam pattern under the spherical-wave effect. Specifically, we derive a closed-form expression for the lobe beamwidth under energy-splitting, revealing a structured and predictable spatial distribution that governs near-field channels in the DFT domain.
- **Physically-informed kernel design and adaptive support discovery:** Leveraging our derived beamwidth analysis, we design a physically-motivated kernel for a Gaussian Process bandit defined over the DFT beam indices. This bandit-based policy enables an intelligent, low-overhead search for the dominant channel support (i.e., significant paths) using only non-coherent, amplitude-only measurements, significantly outperforming other baselines.
- **Rician-aware amplitude-only recovery:** We tailor the Gaussian bandit updates and the sparse phase retrieval refinement to the specific statistics of beam training. By incorporating a Rician denoising step, our framework explicitly accounts for the distribution of amplitude-only feedback in the presence of complex Gaussian noise. This adaptation yields superior reconstruction accuracy and robustness compared to conventional PR solvers that assume simplistic Gaussian noise models. Moreover, by coupling high-probability sub-Gaussian noise proxy induced by our Rician debiasing with the designed kernel prior, the Stage I procedure admits an agnostic GP-bandit (RKHS) justification [27].

The remainder of this paper is organized as follows. Section II introduces the near-field signal model and the amplitude-only measurement formulation. Section III analyzes the near-field channel beam pattern in the DFT space, facilitating the design of our specialized kernel. Section IV presents the proposed framework, detailing the bandit-assisted support discovery and the sparse PR refinement with Gaussian-masked DFT sensing. Section V provides comprehensive simulation results, and Section VI concludes the paper.

Notation: Scalars, vectors, and matrices are denoted by a , \mathbf{a} , and \mathbf{A} . $(\cdot)^T$ and $(\cdot)^H$ denote transpose and conjugate transpose. $\|\cdot\|_2$ is the Euclidean norm and $\|\cdot\|_0$ counts nonzero entries. \otimes denotes the Kronecker product and $\Re\{\cdot\}$ denotes the real part. $[x]_+ \triangleq \max\{x, 0\}$ and $\mathcal{H}_k(\cdot)$ keeps the k largest-magnitude entries. $|\mathcal{S}|$ denotes set cardinality and \mathcal{S}^c denotes set complement. $\mathcal{CN}(\mu, \Sigma)$ and $\mathcal{U}[a, b]$ denote complex Gaussian and uniform distributions, respectively.

II. SYSTEM MODEL

We study a downlink narrowband scenario where a base station (BS) equipped with an $N_y \times N_z$ UPA serves a single-

antenna user. The UPA is placed on the y - z plane and centered at the origin. Let f_c denote the carrier frequency and $\lambda = c/f_c$ the wavelength, where c is the speed of light. The considered geometry is illustrated in Fig. 1.

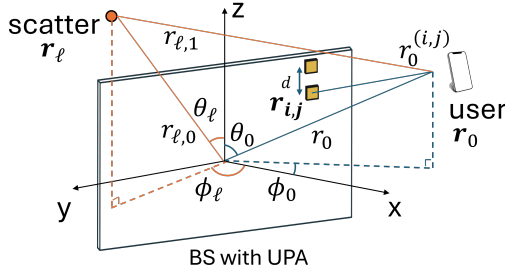


Fig. 1. Diagram of the near-field communication system featuring a UPA.

Let $\mathcal{N}_y \triangleq \{0, 1, \dots, N_y - 1\}$, $\mathcal{N}_z \triangleq \{0, 1, \dots, N_z - 1\}$, and define the centered index offsets $\delta_i \triangleq \frac{2i - N_y + 1}{2}$, $\delta_j \triangleq \frac{2j - N_z + 1}{2}$, $i \in \mathcal{N}_y$, $j \in \mathcal{N}_z$. The (i, j) -th antenna element is located at $\mathbf{r}_{i,j} = (0, \delta_i d, \delta_j d)^\top$, where $d = \lambda/2$ is the inter-element spacing and $N \triangleq N_y N_z$ is the total number of antennas.

A point in space (user or scatterer) is parameterized by spherical coordinates: range $r > 0$, elevation $\theta \in [0, \pi]$, and azimuth $\phi \in [-\pi, \pi]$. We use the unit direction vector

$$\mathbf{q}(\theta, \phi) \triangleq \begin{bmatrix} \sin \theta \cos \phi \\ \sin \theta \sin \phi \\ \cos \theta \end{bmatrix}, \quad (1)$$

so that the corresponding Cartesian position is $r \mathbf{q}(\theta, \phi)$. The distance from this point to the (i, j) -th array element is $r^{(i,j)}(\theta, \phi, r) = \|\mathbf{r} \mathbf{q}(\theta, \phi) - \mathbf{r}_{i,j}\|_2$. Accordingly, the near-field steering response associated with this path is

$$[b(\theta, \phi, r)]_{i,j} = \frac{1}{\sqrt{N}} \exp\left(-j \frac{2\pi}{\lambda} (r^{(i,j)}(\theta, \phi, r) - r)\right), \quad (2)$$

and stacking all (i, j) entries in a fixed order gives the steering vector $\mathbf{b}(\theta, \phi, r) \in \mathbb{C}^N$.

We place the user at (θ_0, ϕ_0, r_0) , where r_0 is the BS-user distance. The line-of-sight (LoS) component is modeled as

$$\mathbf{h}_0 = \sqrt{N} g_0 e^{-j \frac{2\pi r_0}{\lambda}} \mathbf{b}(\theta_0, \phi_0, r_0), \quad (3)$$

with the large-scale gain $g_0 = \frac{\lambda}{4\pi r_0}$.

In addition to LoS, we consider $(L - 1)$ single-bounce scatterers indexed by $\ell = 1, \dots, L - 1$. The ℓ -th scatterer is located at $(\theta_\ell, \phi_\ell, r_{\ell,0})$ relative to the BS, with position $\mathbf{r}_\ell \triangleq r_{\ell,0} \mathbf{q}(\theta_\ell, \phi_\ell)$. The BS-scatterer distance is $r_{\ell,0} = \|\mathbf{r}_\ell\|_2$, and the scatterer-user distance is $r_{\ell,1} = \|\mathbf{r}_0 \mathbf{q}(\theta_0, \phi_0) - \mathbf{r}_\ell\|_2$. The resulting NLoS contribution is

$$\mathbf{h}_\ell = \sqrt{N} g_\ell e^{-j \frac{2\pi(r_{\ell,0} + r_{\ell,1})}{\lambda}} \mathbf{b}(\theta_\ell, \phi_\ell, r_{\ell,0}), \quad (4)$$

where $g_\ell = \frac{\lambda}{4\pi r_{\ell,0} r_{\ell,1}} p_\ell$ and $p_\ell \sim \mathcal{CN}(0, 1)$ capture the two-hop path loss and the random complex reflection coefficient, respectively. Collecting all paths, the downlink channel is

$$\mathbf{h} = \mathbf{h}_0 + \sum_{\ell=1}^{L-1} \mathbf{h}_\ell \in \mathbb{C}^N. \quad (5)$$

In this work, our focus is the near-field regime, in which the user range falls between the Fresnel distance r_F and the Rayleigh distance r_R [28]. Here $r_F \triangleq 0.62 \sqrt{D^3/\lambda}$ and $r_R \triangleq 2D^2/\lambda$, where D is the effective aperture size of the UPA.

III. BEAM PATTERN AND SPARSITY ON UPA

This section characterizes how a near-field path appears in the 2D DFT beamspace of a UPA. In far-field beamspace, the energy of a single path is typically concentrated around one DFT index. In the near field, however, the Fresnel (quadratic) phase induces energy spreading across neighboring DFT indices. More importantly for our design, this spreading exhibits strong axis-aligned locality: due to the separable structure of the Fresnel phase on a UPA, the beamspace power map becomes highly correlated along the two DFT axes, forming a cross-shaped local correlation pattern around the dominant beam. To make this behavior explicit, we first introduce a separable Fresnel approximation under which the UPA response factorizes into two 1D patterns, and then use the 6-dB lobe-width law for near-field ULAs in [29] to quantify the per-axis spreading widths and the resulting effective sparsity.

We parameterize the 2D DFT beamspace using $u \triangleq \sin \theta \sin \phi$, $v \triangleq \cos \theta$. With this choice, the orthogonal 2D DFT sampling corresponds to uniform grids over (u, v) : $u_n = \frac{2n - N_y + 1}{N_y}$, $v_m = \frac{2m - N_z + 1}{N_z}$, for $n \in \{0, \dots, N_y - 1\}$ and $m \in \{0, \dots, N_z - 1\}$.

We use the standard DFT codebook as the beamspace basis on the UPA. Along the y -axis, for any spatial cosine $u \in [-1, 1]$, define the unit-norm 1D DFT vector

$$\mathbf{a}_y(u) \triangleq \frac{1}{\sqrt{N_y}} [e^{-j \frac{2\pi}{\lambda} u \delta_0}, e^{-j \frac{2\pi}{\lambda} u \delta_1}, \dots, e^{-j \frac{2\pi}{\lambda} u \delta_{N_y-1}}]^\top, \quad (6)$$

and similarly along the z -axis

$$\mathbf{a}_z(v) \triangleq \frac{1}{\sqrt{N_z}} [e^{-j \frac{2\pi}{\lambda} v \delta_0}, e^{-j \frac{2\pi}{\lambda} v \delta_1}, \dots, e^{-j \frac{2\pi}{\lambda} v \delta_{N_z-1}}]^\top, \quad (7)$$

A 2D DFT codeword pointing to (u_n, v_m) is then $\mathbf{a}(u_n, v_m) \triangleq \mathbf{a}_y(u_n) \otimes \mathbf{a}_z(v_m) \in \mathbb{C}^{N_y N_z}$.

A. Separable Fresnel approximation

Let $r^{(i,j)}$ be the distance from element (i, j) to a path at (θ, ϕ, r) . A second-order (Fresnel) expansion around the array center gives

$$\begin{aligned} r^{(i,j)} - r &\approx -d(u \delta_i + v \delta_j) + \frac{d^2}{2r} \left((1 - u^2) \delta_i^2 + (1 - v^2) \delta_j^2 \right) \\ &\quad - \frac{d^2}{r} uv \delta_i \delta_j. \end{aligned} \quad (8)$$

Following standard large-array UPA analyses [28], the mixed quadratic term $-\frac{d^2}{r} uv \delta_i \delta_j$ is typically much smaller than the axis-wise quadratic terms over the operating near-field region; we therefore neglect it. This yields an approximately separable near-field phase across the two axes, so the steering vector admits

$$\mathbf{b}(u, v, r) \approx \mathbf{b}_y(u, r) \otimes \mathbf{b}_z(v, r), \quad (9)$$

where

$$[\mathbf{b}_y(u, r)]_i = \frac{1}{\sqrt{N_y}} \exp\left\{-j \frac{2\pi}{\lambda} \left(-d u \delta_i + \frac{d^2}{2r} (1 - u^2) \delta_i^2\right)\right\}, \quad (10)$$

$$[\mathbf{b}_z(v, r)]_j = \frac{1}{\sqrt{N_z}} \exp\left\{-j \frac{2\pi}{\lambda} \left(-d v \delta_j + \frac{d^2}{2r} (1 - v^2) \delta_j^2\right)\right\}. \quad (11)$$

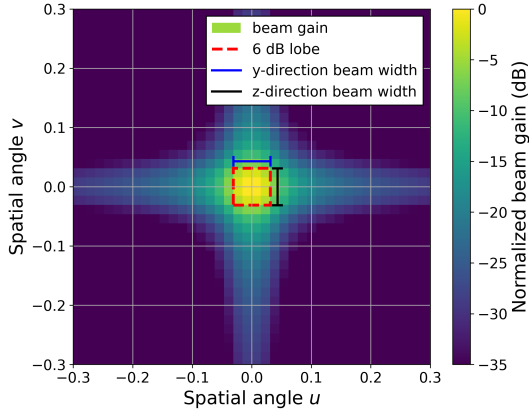


Fig. 2. Normalized DFT-beamspace magnitude on a (128×128) UPA at $f_c = 28$ GHz.

B. 2D beam-pattern factorization and plateau support

Consider a path at (u_0, v_0, r_0) . Under Eq. (9), the inner product between the near-field steering vector and a 2D DFT codeword factorizes as

$$\begin{aligned} G(u_0, v_0, r_0; u_n, v_m) & \\ \triangleq |\mathbf{b}(u_0, v_0, r_0)^H \mathbf{a}(u_n, v_m)| & \\ \approx |\mathbf{b}_y(u_0, r_0)^H \mathbf{a}_y(u_n)| |\mathbf{b}_z(v_0, r_0)^H \mathbf{a}_z(v_m)|. & \end{aligned} \quad (12)$$

Hence, the 2D magnitude response can be understood as the product of two 1D responses, one per axis.

To quantify the 1D spreading, we normalize the axis-wise responses. For the z -axis, define

$$G_{z,\text{norm}}(v_0, r_0; v) \triangleq \frac{|\mathbf{b}_z(v_0, r_0)^H \mathbf{a}_z(v)|}{|\mathbf{b}_z(v_0, r_0)^H \mathbf{a}_z(v_0)|}. \quad (13)$$

The corresponding 6-dB lobe set is

$$\Phi_{6\text{dB}}^z(v_0, r_0) \triangleq \{v \mid G_{z,\text{norm}}(v_0, r_0; v) \geq 1/2\}, \quad (14)$$

and its width is

$$B_z(v_0, r_0) \triangleq \max(\Phi_{6\text{dB}}^z) - \min(\Phi_{6\text{dB}}^z). \quad (15)$$

The same definitions apply to the y -axis.

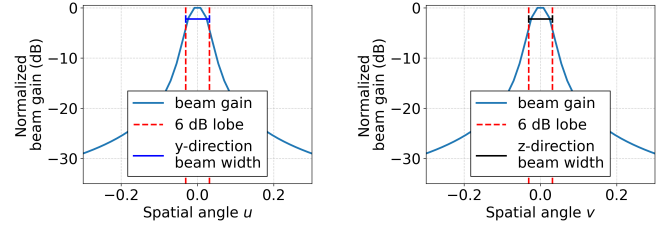
For near-field ULAs, [29] shows that the 6-dB lobe width for a path at (ξ_0, r_0) admits

$$B(\xi_0, r_0) = Nd \frac{1 - \xi_0^2}{r_0}. \quad (16)$$

In our UPA model, Eq. (11) reveals that $\mathbf{b}_y(u_0, r_0)$ and $\mathbf{b}_z(v_0, r_0)$ share the same quadratic-phase structure as the ULA steering vector in [29], but with apertures $N_y d$ and $N_z d$. Applying the same 6-dB width law along each axis yields

$$B_y(u_0, r_0) = N_y d \frac{1 - u_0^2}{r_0}, \quad B_z(v_0, r_0) = N_z d \frac{1 - v_0^2}{r_0}. \quad (17)$$

These widths quantify the extent of near-field energy spreading around the peak in the continuous (u, v) domain. Combined with the factorization in Eq. (12), a convenient support approximation is to take the Cartesian product of the two axis-wise 6-dB sets, which aligns with the connected plateau with sharp edges observed in 2D DFT beamspace [9], [29].



(a) u-cut (y-direction beam width) (b) v-cut (z-direction beam width)

Fig. 3. 1D cuts of the normalized gain and the 6-dB lobe widths.

An example of the UPA beam pattern is shown in Fig. 2. The red dashed rectangle marks a 6-dB support region, which serves as a convenient approximation for the effective active neighborhood. Fig. 3 further reports the 1D u - and v -cuts through the peak of Fig. 2; the 6-dB thresholds delineate the per-axis lobe widths B_y and B_z . Together with the factorization in Eq. (12), these cuts highlight strong axis-aligned locality, i.e., nearby DFT indices along the u - and v -directions tend to have similar magnitudes, giving rise to the cross-shaped correlation pattern.

C. Effective sparsity level in 2D DFT beamspace

Let Δ_y and Δ_z denote the DFT grid spacings along the u - and v -axes, respectively. Approximating each path's 2D lobe support by a rectangle with side lengths B_y and B_z , the number of active DFT coefficients per path is approximately $B_y B_z / (\Delta_y \Delta_z)$. For L paths with non-overlapping lobe supports (the worst case), the expected sparsity level K_{UPA} (i.e., the expected number of active DFT coefficients) scales as

$$\mathbb{E}[K_{\text{UPA}}] \approx \frac{LN_y N_z d^2}{\Delta_y \Delta_z} \mathbb{E}\left[\frac{(1-u^2)(1-v^2)}{r^2}\right]. \quad (18)$$

Note that u and v are coupled through $u = \sin \theta \sin \phi = \sqrt{1-v^2} s$ with $s \triangleq \sin \phi$. We assume the following independent uniform distributions:

$$v = \cos \theta \sim \mathcal{U}[v_1, v_2], \quad s = \sin \phi \sim \mathcal{U}[s_1, s_2], \quad r \sim \mathcal{U}[r_1, r_2], \quad (19)$$

and v, s, r are independent to each other. Then the expectation in Eq. (18) admits a closed form, and the sparsity approximation becomes

$$\mathbb{E}[K_{\text{UPA}}] \approx \frac{LN_y N_z d^2}{\Delta_y \Delta_z} (\Xi_{v,s}) (\Xi_r), \quad (20)$$

where

$$\Xi_r = \frac{1}{r_2 - r_1} \left(\frac{1}{r_1} - \frac{1}{r_2} \right), \quad (21)$$

$$\Xi_{v,s} = (1 - \mu_2) - \nu_2 (1 - 2\mu_2 + \mu_4), \quad (22)$$

with the moments

$$\begin{aligned} \mu_2 &= \frac{v_2^3 - v_1^3}{3(v_2 - v_1)}, \quad \mu_4 = \frac{v_2^5 - v_1^5}{5(v_2 - v_1)}, \\ \nu_2 &= \frac{s_2^3 - s_1^3}{3(s_2 - s_1)}. \end{aligned} \quad (23)$$

A detailed derivation of Eq. (20) is provided in Appendix A. For a $N_y \times N_z = 128 \times 16$ UPA at $f_c = 28$ GHz with $d = \lambda/2$ and the standard 2D DFT grid $\Delta_y = 2/N_y$ and $\Delta_z = 2/N_z$,

consider $v \sim \mathcal{U}[-\frac{1}{2}, \frac{1}{2}]$, $s \sim \mathcal{U}[-\frac{1}{2}, \frac{1}{2}]$, $r \sim \mathcal{U}[r_F, \frac{r_R}{20}]$. In this case, for an $L = 6$ -path channel, Eq. (18) yields $\mathbb{E}[K_{\text{UPA}}] \approx 11$, confirming that the near-field channel remains strongly sparse in the 2D DFT beamspace under this setting. Moreover, the preceding analysis implies pronounced cross-shaped local correlation of DFT-beam magnitudes around only a few dominant components. In the sequel, we exploit this structure to design a cross-pattern kernel for Stage I search and to justify sparse recovery over the standard 2D DFT codebook for Stage II PR.

IV. PROPOSED GAUSSIAN BANDIT-ASSISTED SPARSE PHASE RETRIEVAL

This section presents a two-stage amplitude-only near-field beam training framework for UPAs, which operates in the DFT beamspace. Stage I performs adaptive support discovery by sequentially probing a small subset of 2D DFT beams and using a GP bandit to learn the beamspace power over the DFT grid. The key idea is to exploit the structured near-field DFT beam pattern characterized in Section III: due to near-field energy splitting, neighboring DFT indices exhibit locally correlated magnitudes within a compact lobe region, which motivates a smooth GP prior and enables an efficient adaptive search. Stage II then refines the channel estimate by performing sparse phase retrieval over the discovered support set in Stage I using a Gaussian-masked DFT sensing matrix. By restricting the search space, Stage II operates on a much lower ambient dimension and thus requires fewer amplitude measurements than a full-grid recovery, while still being able to further prune and refine the support locally.

A. Stage I: GP-LSE Support Discovery in 2D DFT Beamspace

Let $\mathcal{I} \triangleq \{(n, m) : n \in \{0, \dots, N_y - 1\}, m \in \{0, \dots, N_z - 1\}\}$ denote the 2D DFT beam index set. For each $i = (n, m) \in \mathcal{I}$, let $\mathbf{f}_i \in \mathbb{C}^N$ denote the corresponding unit-norm 2D DFT codeword on the UPA (i.e., the beam pointing to the DFT grid point (u_n, v_m) introduced in Section III). During Stage I, the BS restricts its probing beams to this DFT codebook. Specifically, at training slot t , the BS transmits a known pilot x_t (with $|x_t| = 1$) using the i_t -th DFT beamforming vector $\mathbf{v}_{i_t} = \mathbf{f}_{i_t}$, $i_t = (n_t, m_t) \in \mathcal{I}$. The received signal at the user is

$$y_t = \mathbf{h}^H \mathbf{v}_{i_t} x_t + w_t, \quad w_t \sim \mathcal{CN}(0, \sigma^2). \quad (24)$$

Due to phase impairments, we use the power feedback $z_t^{\text{raw}} = |y_t|^2$ and define the beamspace power map $f(i) \triangleq |\mathbf{h}^H \mathbf{f}_i|^2$. Since $\mathbb{E}[z_t^{\text{raw}} | \mathbf{h}] = f(i_t) + \sigma^2$, we subtract the noise bias and obtain

$$\tilde{z}_t \triangleq z_t^{\text{raw}} - \sigma^2 = f(i_t) + \tilde{\varepsilon}_t, \quad (25)$$

where $\tilde{\varepsilon}_t$ is conditionally zero-mean and captures the fluctuation of the noncentral Rician power around its mean. For tractable GP regression, we compute $(\mu_t(\cdot), \sigma_t^2(\cdot))$ using the standard Gaussian-likelihood GP update with regularization parameter σ_ε^2 in Eq. (31). Notably, the debiased power noise $\tilde{\varepsilon}_t$ in Eq. (25) is generally non-Gaussian. To enable high-probability confidence statements, we construct in Appendix B a bounded-noise event $\mathcal{E}_{\text{bd}}(T_1)$ such that, with probability at least $1 - \delta_{\text{bd}}$, the feedback noise forms a uniformly bounded martingale difference sequence over the Stage I horizon:

$|\tilde{\varepsilon}_t| \leq B_t \leq B_{T_1}$ for all $t \leq T_1$. This bounded-noise model is then used in Appendix C to derive the GP-LSE guarantee via Theorem 6 of [27].

We place a GP prior on the power map $f(\cdot)$:

$$f(\cdot) \sim \mathcal{GP}(0, k(\cdot, \cdot)). \quad (26)$$

Motivated by the empirical near-field DFT beam pattern in Fig. 2, the beamspace power map inherits a compact plateau around the peak and a cross-shaped correlation along the two DFT axes. In particular, if a given DFT beam exhibits a large received power, then its neighboring beams along the u - and v -directions are also likely to be strong due to near-field energy spreading. To encode this physics-driven coupling, so that each probed beam can inform a cross-shaped neighborhood of unprobed beams, we adopt a *cross-pattern* kernel defined on the 2D DFT coordinates.

Associate each index $i = (n, m)$. We define the 1D Laplacian kernels

$$k_u(i, i') = \exp\left(-\frac{|u_n - u_{n'}|}{\ell_u}\right), \quad k_v(i, i') = \exp\left(-\frac{|v_m - v_{m'}|}{\ell_v}\right), \quad (27)$$

and construct a *cross-pattern* combination

$$k(i, i') = \alpha \frac{k_u(i, i') + k_v(i, i')}{2} + (1 - \alpha) k_u(i, i') k_v(i, i'), \quad (28)$$

where $\alpha \in [0, 1]$ trades off axis-aligned (cross-shaped) correlation vs. joint 2D correlation, and ℓ_u, ℓ_v control the correlation span along the y - and z -axes, respectively. To reflect the near-field beamwidth law Eq. (17), a physics-guided choice links (ℓ_u, ℓ_v) to typical lobe widths,

$$\ell_u = \kappa_u \bar{B}_y, \quad \ell_v = \kappa_v \bar{B}_z, \quad (29)$$

$$\bar{B}_y \triangleq N_y d \mathbb{E}\left[\frac{1 - u^2}{r}\right], \quad \bar{B}_z \triangleq N_z d \mathbb{E}\left[\frac{1 - v^2}{r}\right], \quad (30)$$

where the expectations are taken under the angle and distance priors and (κ_u, κ_v) are tunable constants. If such priors are not available, one can directly tune ℓ_u and ℓ_v .

Let $\mathcal{D}_t = \{(i_s, \tilde{z}_s)\}_{s=1}^t$ denote the denoised observations up to slot t , and collect $\tilde{\mathbf{z}}_t = [\tilde{z}_1, \dots, \tilde{z}_t]^\top$. Define the kernel matrix $\mathbf{K}_t \in \mathbb{R}^{t \times t}$ with $[\mathbf{K}_t]_{a,b} = k(i_a, i_b)$, and

$$\tilde{\mathbf{K}}_t \triangleq \mathbf{K}_t + \sigma_\varepsilon^2 \mathbf{I}_t. \quad (31)$$

Here σ_ε^2 is an effective regularization parameter used by the GP posterior update: it absorbs model mismatch and controls how strongly the posterior interpolates the observed debiased power feedback. In the analysis, a conservative choice is $\sigma_\varepsilon^2 \gtrsim B_{T_1}^2$ on the bounded-noise event in Appendix B.

For any candidate beam $i \in \mathcal{I}$, define the kernel vector

$$\mathbf{k}_t(i) \triangleq [k(i, i_1), \dots, k(i, i_t)]^\top. \quad (32)$$

Then the GP posterior on $f(i)$ is Gaussian with the following mean value and variance

$$\mu_t(i) = \mathbf{k}_t(i)^\top \tilde{\mathbf{K}}_t^{-1} \tilde{\mathbf{z}}_t, \quad (33)$$

$$\sigma_t^2(i) = k(i, i) - \mathbf{k}_t(i)^\top \tilde{\mathbf{K}}_t^{-1} \mathbf{k}_t(i). \quad (34)$$

After each new probe (i_t, \tilde{z}_t) , we augment the dataset \mathcal{D}_t and update the GP posterior by recomputing the mean and

TABLE I
TYPICAL GROWTH OF γ_t FOR COMMON KERNELS ON A COMPACT DOMAIN.

Kernel family	Order of γ_t
Linear	$\mathcal{O}(d \log t)$
Squared Exponential	$\mathcal{O}((\log t)^{d+1})$
Matérn	$\mathcal{O}\left(t^{\frac{d(d+1)}{2\nu+d(d+1)}} \log t\right)$

variance according to Eq. (33)-Eq. (34). Note that the GP prior is defined on the finite DFT index set \mathcal{I} , and the time index t merely labels the sequential observations. Multiple probes of the same beam index $i \in \mathcal{I}$ therefore correspond to multiple noisy samples of the same latent value $f(i)$, which are naturally handled by the GP posterior update.

Based on the GP posterior in Eq. (33)-Eq. (34), we adopt the Gaussian-process level-set estimation (GP-LSE) principle to guide adaptive DFT probing [30]. The goal of Stage I is to efficiently identify a candidate set of promising DFT beams with significant received powers (i.e., support) based on a limited probing budget T_1 .

At round $t+1$, define the GP confidence interval for each $i \in \mathcal{I}$ as

$$Q_{t+1}(i) \triangleq \left[\mu_t(i) - \sqrt{\beta_{t+1}} \sigma_t(i), \mu_t(i) + \sqrt{\beta_{t+1}} \sigma_t(i) \right], \quad (35)$$

where β_t is a nondecreasing exploration schedule. For our theoretical guarantee under the non-Gaussian debiased power noise, Appendix C invokes the bounded-noise RKHS confidence schedule from Theorem 6 of [27]:

$$\beta_t = 2B_f^2 + 300 \gamma_{t-1} \log^3\left(\frac{t}{\delta}\right), \quad t \geq 1, \quad (36)$$

where $\|f\|_{\mathcal{H}_k} \leq B_f$ (see Appendix C) and γ_t is the maximum information gain induced by k . The quantity γ_t is the maximum information gain of the kernel k over the finite index set \mathcal{I} , i.e., the largest mutual information between t noisy samples and the latent function values that can be achieved by the best choice of t query locations:

$$\gamma_t \triangleq \max_{A \subseteq \mathcal{I}, |A|=t} \frac{1}{2} \log \det(\mathbf{I}_t + \sigma_\varepsilon^{-2} \mathbf{K}_A), \quad (37)$$

where \mathbf{K}_A is the Gram matrix on A with entries $k(\cdot, \cdot)$. Intuitively, γ_t quantifies the *intrinsic statistical complexity* of learning f under the similarity notion induced by k : faster spectral decay yields smaller γ_t , hence fewer probes are needed to shrink GP confidence intervals. Some examples can be found in Table I [27]. Since each 1D Laplace factor k_u (and k_v) is the Matérn kernel with smoothness $\nu = \frac{1}{2}$, the product term in Eq. (28) is a separable 2D Matérn (also $\nu = \frac{1}{2}$) kernel, and the overall plus-Laplace kernel is its convex combination with an additive term. Thus, combining [27, Theorem 4] and the Matérn spectral-decay bound in [27, Theorem 5], the worst-case γ_t for our kernel follows by specializing the Matérn bound at $\nu = \frac{1}{2}$. Here d denotes the dimension of the kernel input space and, in our Stage I GP over the 2D DFT grid, $d = 2$. While Eq. (36) involves quantities that are not available in closed form in practice, it is standard in kernelized bandit implementations to treat these terms as tunable conservatism parameters that control the exploration-exploitation tradeoff.

Following [30], we maintain a monotonically shrinking confidence region by intersecting intervals over time:

$$\begin{aligned} \ell_{t+1}(i) &\triangleq \max\{\ell_t(i), \mu_t(i) - \sqrt{\beta_{t+1}} \sigma_t(i)\}, \\ u_{t+1}(i) &\triangleq \min\{u_t(i), \mu_t(i) + \sqrt{\beta_{t+1}} \sigma_t(i)\}, \end{aligned} \quad (38)$$

initialized with $\ell_0(i) = -\infty$ and $u_0(i) = +\infty$. These bounds summarize all information collected up to time t and are tighter than the raw GP interval Eq. (35).

Specifically, fix a power threshold $\tau > 0$ and a tolerance $\epsilon > 0$. We then perform level-set classification with tolerance ϵ :

$$\mathcal{H}_{t+1} \triangleq \mathcal{H}_t \cup \{i \in \mathcal{I} : \ell_{t+1}(i) > \tau - \epsilon\}, \quad (39)$$

$$\mathcal{L}_{t+1} \triangleq \mathcal{L}_t \cup \{i \in \mathcal{I} : u_{t+1}(i) \leq \tau + \epsilon\}, \quad (40)$$

$$\mathcal{U}_{t+1} \triangleq \mathcal{I} \setminus (\mathcal{H}_{t+1} \cup \mathcal{L}_{t+1}), \quad (41)$$

where \mathcal{H}_t collects indices predicted to be above the threshold (candidate strong beams), \mathcal{L}_t collects indices predicted to be below, and \mathcal{U}_t are the remaining undecided indices that concentrate around the boundary.

To decide the next probing beam, GP-LSE selects the most ambiguous undecided index [30]. Define the ambiguity score

$$a_{t+1}(i) \triangleq \min\{u_{t+1}(i) - \tau, \tau - \ell_{t+1}(i)\}, \quad i \in \mathcal{U}_{t+1}, \quad (42)$$

and choose

$$i_{t+1} \in \arg \max_{i \in \mathcal{U}_{t+1}} a_{t+1}(i). \quad (43)$$

After probing i_{t+1} , we obtain \tilde{z}_{t+1} via Eq. (25), update the GP posterior Eq. (33)-Eq. (34), and repeat until we reach the Stage I budget T_1 or when $\max_{i \in \mathcal{U}_t} a_t(i) \leq \epsilon$.

1) Stage I outputs support for Stage II.

Suppose we have T_1 adaptive probes in total, the GP-LSE procedure then produces a confidence-aware partition of the DFT index set into the predicted superlevel set \mathcal{H}_{T_1} , the predicted sublevel set \mathcal{L}_{T_1} , and the remaining undecided set \mathcal{U}_{T_1} in Eq. (39)-Eq. (41). In the ideal LSE setting, the natural output is the entire superlevel set

$$\widehat{\mathcal{S}}_{\text{LSE}} \triangleq \mathcal{H}_{T_1}, \quad (44)$$

which has an *adaptive cardinality*: as the posterior confidence region shrinks around the threshold τ , indices whose power is confidently above τ are accumulated in \mathcal{H}_{T_1} , while those confidently below τ are discarded into \mathcal{L}_{T_1} [30]. Therefore, $|\widehat{\mathcal{S}}_{\text{LSE}}|$ is automatically adjusted to the observed beamspace power profile, which is desirable for multi-path channels where the effective support size can vary across physical environments and frequency bands.

2) Stage I overhead in terms of information gain.

Under the bounded-noise event $\mathcal{E}_{\text{bd}}(T_1)$ in Appendix B and the RKHS condition $\|f\|_{\mathcal{H}_k} \leq B_f$, the GP-LSE ambiguity $\max_{i \in \mathcal{U}_t} a_t(i)$ drops below ϵ after a number of probes characterized by the information gain of kernel k [27], [30]. In particular, using the Theorem 6 exploration schedule Eq. (36), a sufficient condition for termination is

$$T_1 = \tilde{\mathcal{O}}\left(\frac{\beta_{T_1} \gamma_{T_1}}{\epsilon^2}\right) = \tilde{\mathcal{O}}\left(\frac{B_f^2 \gamma_{T_1} + \gamma_{T_1}^2}{\epsilon^2}\right). \quad (45)$$

Equivalently, when the algorithm is run until the stopping condition $\max_{i \in \mathcal{U}_t} a_t(i) \leq \epsilon$ (or $\mathcal{U}_t = \emptyset$) is met, the resulting level-set estimate satisfies the standard ϵ -accurate inclusion

$$\{i : f(i) \geq \tau + \epsilon\} \subseteq \mathcal{H}_t \subseteq \{i : f(i) \geq \tau - \epsilon\} \quad (46)$$

with probability at least $1 - (\delta_{\text{bd}} + \delta)$. A self-contained derivation of Eq. (46) and Eq. (45) is provided in Appendix C.

3) Practical support truncation under a fixed probing budget

In principle, GP-LSE can be run until all indices are classified, i.e., $\mathcal{U}_t = \emptyset$, or until the ambiguity vanishes, $\max_{i \in \mathcal{U}_t} a_t(i) \leq \epsilon$ [30]. However, in practical beam training we operate under a fixed probing budget T_1 , and it is possible that a small residual undecided set remains, i.e., $\mathcal{U}_{T_1} \neq \emptyset$, because the algorithm has not yet fully separated all beams into \mathcal{H}_{T_1} or \mathcal{L}_{T_1} . In this case, we apply a lightweight *fallback patch* to produce a fixed-cardinality support for Stage II: we retain the confidently strong beams in \mathcal{H}_{T_1} , and then augment/truncate using the posterior mean ranking. Concretely, if $\mathcal{U}_{T_1} = \emptyset$, we directly set $\hat{\mathcal{S}} = \mathcal{H}_{T_1}$. Otherwise, when $\mathcal{U}_{T_1} \neq \emptyset$, we form

$$\hat{\mathcal{S}} \triangleq \text{Top-}K\left(\{\mu_{T_1}(i) : i \in \mathcal{H}_{T_1} \cup \mathcal{U}_{T_1}\}\right), \quad (47)$$

where $\text{Top-}K(\cdot)$ returns the indices of the K largest values. This patch is *not* used when GP-LSE has already completed the classification; it is only invoked to handle the fixed-budget setting and to guarantee a well-defined, computationally manageable support size for the Stage II Gaussian-masked sensing and sparse PR refinement. The parameter K can be selected using the sparsity characterization in Section III or treated as a design parameter trading refinement complexity and robustness. At this point, we stop exploring and convert the learned posterior into a support estimate.

B. Stage II: Gaussian-Masked DFT Sensing and Rician-SPARTA Refinement

Following the completion of Stage I, the BS has identified an estimate of the dominant DFT-beam support $\hat{\mathcal{S}} \subset \mathcal{I}$, where $|\hat{\mathcal{S}}| = K \ll N$. We define the transformation matrix

$$\mathbf{F} \triangleq [\mathbf{f}_{0,0}, \dots, \mathbf{f}_{N_y-1, N_z-1}]^H \in \mathbb{C}^{N \times N}. \quad (48)$$

as the collection of all unit-norm 2D DFT beams as rows, ordered according to \mathcal{I} . Under this representation, the DFT beamspace coefficients are given by $\mathbf{s} = \mathbf{F}\mathbf{h}$, with the inverse relation $\mathbf{h} = \mathbf{F}^H \mathbf{s}$. Let $\mathbf{F}_{\hat{\mathcal{S}}} \in \mathbb{C}^{K \times N}$ denote the submatrix consisting of rows of \mathbf{F} indexed by $\hat{\mathcal{S}}$, and let $\mathbf{s}_{\hat{\mathcal{S}}} \in \mathbb{C}^K$ be the corresponding beamspace coefficients. As characterized in Section III, the channel can be approximated within this reduced subspace as:

$$\mathbf{h} \approx \mathbf{F}_{\hat{\mathcal{S}}}^H \mathbf{s}_{\hat{\mathcal{S}}}, \quad \|\mathbf{s}_{\hat{\mathcal{S}}}\|_0 \leq K, \quad (49)$$

with sparsity level K .

In Stage II, the BS constructs a second set of M_2 pilot beams by linearly combining only the DFT beams within the estimated support $\hat{\mathcal{S}}$. For each measurement index $p = 1, \dots, M_2$, we draw an i.i.d. complex Gaussian mask $\mathbf{g}_p \sim \mathcal{CN}(\mathbf{0}, \frac{1}{K} \mathbf{I}_K)$ and synthesize the Gaussian-masked DFT beam:

$$\mathbf{v}_p = \mathbf{F}_{\hat{\mathcal{S}}}^H \mathbf{g}_p \in \mathbb{C}^N. \quad (50)$$

The BS transmits a unit-modulus pilot through \mathbf{v}_p , and the user feeds back only the received amplitude (or power). The resulting amplitude-only observation at slot p is

$$y_p = |\mathbf{h}^H \mathbf{v}_p + w_p|, \quad w_p \sim \mathcal{CN}(0, \sigma^2), \quad (51)$$

where y_p follows a Rician distribution with non-centrality parameter $|\mathbf{h}^H \mathbf{v}_p|$. By substituting Eq. (49) and Eq. (50) into Eq. (51), we obtain an equivalent low-dimensional beamspace model:

$$y_p = |\mathbf{s}_{\hat{\mathcal{S}}}^H \mathbf{g}_p + w_p|, \quad p = 1, \dots, M_2. \quad (52)$$

Hence, Stage II reduces to recovering the sparse beamspace vector $\mathbf{s}_{\hat{\mathcal{S}}}$ from Rician-corrupted magnitude measurements with i.i.d. complex Gaussian sensing vectors $\{\mathbf{g}_p\}_{p=1}^{M_2}$.

Directly applying standard PR solvers to y_p often leads to performance degradation due to the bias introduced by the noise in the magnitude domain. To mitigate this, we observe that $\mathbb{E}[y_p^2 | \mathbf{g}_p] = |\mathbf{s}_{\hat{\mathcal{S}}}^H \mathbf{g}_p|^2 + \sigma^2$. We therefore perform Rician denoising by defining the pseudo-amplitude $\tilde{\psi}_p$:

$$\tilde{\psi}_p \triangleq \sqrt{[y_p^2 - \sigma^2]_+}. \quad (53)$$

The resulting $\tilde{\psi}_p$ serves as a pseudo-amplitude that approximates $|\mathbf{s}_{\hat{\mathcal{S}}}^H \mathbf{g}_p|$ while absorbing the residual Rician fluctuations into an effective noise term. This yields an amplitude-based sparse PR model of the form

$$\tilde{\psi}_p = |\mathbf{s}_{\hat{\mathcal{S}}}^H \mathbf{g}_p| + \tilde{\eta}_p, \quad p = 1, \dots, M_2, \quad (54)$$

i.e., in our setting, we apply the Rician debiasing and the pseudo-amplitude mapping Eq. (53), which yields an equivalent noisy-amplitude model Eq. (54) (see proof in Appendix D). Therefore, Stage II can be viewed as running a robust truncated amplitude-flow solver on noisy amplitudes [24].

Given the denoised amplitudes $\{\tilde{\psi}_p\}$ and sensing vectors $\{\mathbf{g}_p\}$, we seek a k -sparse estimate of $\mathbf{s}_{\hat{\mathcal{S}}}$ by minimizing an amplitude-based least-squares loss subject to sparsity:

$$\min_{\mathbf{z} \in \mathbb{C}^K} \frac{1}{M_2} \sum_{p=1}^{M_2} (\tilde{\psi}_p - |\mathbf{g}_p^H \mathbf{z}|)^2 \quad \text{s.t.} \quad \|\mathbf{z}\|_0 \leq k \leq K. \quad (55)$$

We adopt a SPARTA-style solver[24] that combines truncated amplitude-based gradient steps with hard thresholding, but with two modifications tailored to our setting: (i) the algorithm operates only on the reduced beamspace supported on $\hat{\mathcal{S}}$, and (ii) the amplitudes in Eq. (55) are replaced by the Rician-denoised pseudo-measurements $\tilde{\psi}_p$ in Eq. (53).

Concretely, let $\mathbf{z}^{(0)}$ be an initialization restricted to $\hat{\mathcal{S}}$, which can be got by a scaled principal eigenvector of a sample covariance matrix formed from the largest $\tilde{\psi}_p$'s, and denote $\mathcal{I}_t \subseteq \{1, \dots, M_2\}$ as the truncation set at iteration t , which retains only those indices whose amplitude residuals are not too large. A generic Rician-SPARTA refinement iteration takes the form

$$\mathbf{z}^{(t+\frac{1}{2})} = \mathbf{z}^{(t)} - \mu_t \frac{1}{|\mathcal{I}_t|} \sum_{p \in \mathcal{I}_t} \left(|\mathbf{g}_p^H \mathbf{z}^{(t)}| - \tilde{\psi}_p \right) \frac{\mathbf{g}_p \mathbf{g}_p^H \mathbf{z}^{(t)}}{|\mathbf{g}_p^H \mathbf{z}^{(t)}|}, \quad (56)$$

$$\mathbf{z}^{(t+1)} = \mathcal{H}_k(\mathbf{z}^{(t+\frac{1}{2})}), \quad (57)$$

where $\mu_t > 0$ is a stepsize, and $\mathcal{H}_k(\cdot)$ denotes the hard-thresholding operator that keeps the k entries with the largest magnitudes and sets the rest to zero. The truncation rule defining \mathcal{I}_t follows the standard SPARTA design [24], with thresholds applied to the amplitude residuals $|\mathbf{g}_p^H \mathbf{z}^{(t)}| - \tilde{\psi}_p$ to suppress the impact of outliers and residual Rician noise.

After a prescribed number of iterations, we obtain $\hat{\mathbf{s}}_{\hat{\mathcal{S}}} = \mathbf{z}^{(T)}$ and form the final channel estimate

$$\hat{\mathbf{h}} = \mathbf{F}_{\hat{\mathcal{S}}}^H \hat{\mathbf{s}}_{\hat{\mathcal{S}}}, \quad (58)$$

which is then used for downlink beamforming.

Compared with applying SPARTA on the full DFT beamspace directly, the proposed Stage II operates on a much smaller subspace identified by Stage I and incorporates Rician denoising via Eq. (53), thereby reducing both the required number of measurements and the computational cost, while better matching the amplitude-only feedback model in near-field beam training.

Specializing the SPARTA theory [24] to the ambient dimension K (where $K = |\hat{\mathcal{S}}|$ is the size of the discovered index set) implies that an additional M_2 measurements on the order of

$$M_2 \gtrsim C k^2 \log(K) \quad (59)$$

are sufficient for exact recovery with high probability.

Importantly, Stage II probes only $\text{span}(\mathbf{F}_{\hat{\mathcal{S}}}^H)$, hence the noiseless observations depend only on $\mathbf{s}_{\hat{\mathcal{S}}}$ regardless of energy outside $\hat{\mathcal{S}}$. Consequently, for any estimate $\hat{\mathbf{s}}$ supported on $\hat{\mathcal{S}}$ and $\hat{\mathbf{h}} = \mathbf{F}_{\hat{\mathcal{S}}}^H \hat{\mathbf{s}}$, unitarity of \mathbf{F} yields the exact error decomposition

$$\|\hat{\mathbf{h}} - \mathbf{h}\|_2^2 = \|\hat{\mathbf{s}}_{\hat{\mathcal{S}}} - \mathbf{s}_{\hat{\mathcal{S}}}\|_2^2 + \|\mathbf{s}_{\hat{\mathcal{S}}^c}\|_2^2, \quad (60)$$

which separates the algorithmic error on the discovered subspace and the irreducible tail caused by false negatives. False positives primarily enlarge K , thereby increasing the logarithmic term in Eq. (59) and raising computational cost, whereas the tail energy $\|\mathbf{s}_{\hat{\mathcal{S}}^c}\|_2$ imposes a fundamental error floor when K fails to cover the full support set. However, under Stage I, there is a high probability that $\hat{\mathcal{S}}$ coincides with the true dominant DFT support [31]; consequently, the tail term $\|\mathbf{s}_{\hat{\mathcal{S}}^c}\|_2$ in Eq. (60) vanishes.

V. SIMULATION RESULTS

This section evaluates the performance of the proposed two-stage near-field beam training framework through comprehensive numerical simulations. We consider a single BS equipped with a UPA of $N_y = 128$ and $N_z = 16$ antenna elements, operating at a carrier frequency of $f_c = 28$ GHz. The total number of antenna elements is $N = N_y N_z = 2048$. For each method, we reconstruct the channel estimate $\hat{\mathbf{h}}$ and evaluate the normalized correlation:

$$\rho \triangleq \frac{|\mathbf{h}^H \hat{\mathbf{h}}|}{\|\mathbf{h}\|_2 \|\hat{\mathbf{h}}\|_2} \in [0, 1], \quad (61)$$

where $\rho \approx 1$ signifies near-perfect channel recovery. All results are averaged over 500 Monte-Carlo trials.

Algorithm 1 Near-Field Beam Training via GP-LSE Assisted Sparse Phase Retrieval

Input: 2D DFT codebook $\{\mathbf{f}_{n,m}\}$ and transform \mathbf{F} ; budgets (T_1, M_2) ; noise variance σ^2 ; kernel $k(\cdot, \cdot)$; LSE parameters $(\tau, \epsilon, \{\beta_t\})$; sparsity level k for Stage II.

Output: $\hat{\mathcal{S}}, \hat{\mathbf{s}}_{\hat{\mathcal{S}}}, \hat{\mathbf{h}}, \hat{\mathbf{v}}$.

Stage I (GP-LSE on 2D DFT grid): initialize $(\mathcal{H}_0, \mathcal{L}_0, \mathcal{U}_0)$ and $(\ell_0(\cdot), u_0(\cdot))$ as in Eq. (38), with $\mathcal{D}_0 = \emptyset$.

for $t = 1, \dots, T_1$ **do**

 Update GP posterior $(\mu_{t-1}(\cdot), \sigma_{t-1}(\cdot))$ via Eq. (33)-Eq. (34).

 Update $(\ell_t(\cdot), u_t(\cdot))$ and $(\mathcal{H}_t, \mathcal{L}_t, \mathcal{U}_t)$ via Eq. (38)-Eq. (41).

 If $\mathcal{U}_t = \emptyset$ or $\max_{i \in \mathcal{U}_t} a_t(i) \leq \epsilon$ with $a_t(\cdot)$ in Eq. (42), **break**.

 Select $i_t \in \arg \max_{i \in \mathcal{U}_t} a_t(i)$ via Eq. (43), probe $\mathbf{v}_{i_t} = \mathbf{f}_{i_t}$, and form $\tilde{\mathbf{z}}_t$ via Eq. (25).

 Append $(i_t, \tilde{\mathbf{z}}_t)$ to \mathcal{D}_t .

end for

Support: set $\hat{\mathcal{S}} = \mathcal{H}_{\hat{T}_1}$ if $\mathcal{U}_{\hat{T}_1} = \emptyset$, else apply the Top- K patch Eq. (47).

Stage II (Gaussian-masked DFT & Rician-SPARTA): let $K = |\hat{\mathcal{S}}|$ and form $\mathbf{F}_{\hat{\mathcal{S}}}$.

for $p = 1, \dots, M_2$ **do**

 Draw $\mathbf{g}_p \sim \mathcal{CN}(\mathbf{0}, \frac{1}{K} \mathbf{I})$ and set $\mathbf{v}_p = \mathbf{F}_{\hat{\mathcal{S}}}^H \mathbf{g}_p$ Eq. (50).

 Observe y_p in Eq. (51) and compute $\tilde{\psi}_p$ via Eq. (53).

end for

Obtain $\hat{\mathbf{s}}_{\hat{\mathcal{S}}}$ by running the Rician-SPARTA solver defined in Eq. (55) (updates Eq. (56)-Eq. (57)).

Recover $\hat{\mathbf{h}}$ by Eq. (58) and set $\hat{\mathbf{v}} = \hat{\mathbf{h}} / \|\hat{\mathbf{h}}\|_2$.

return $\hat{\mathcal{S}}, \hat{\mathbf{s}}_{\hat{\mathcal{S}}}, \hat{\mathbf{h}}, \hat{\mathbf{v}}$.

A. Performance under Varying SNR

We first assess robustness against additive noise by sweeping the SNR from -15 dB to 15 dB. Specifically, we set the noise power as $\frac{\|\mathbf{h}\|_2^2}{n \text{SNR}}$, and $\text{SNR} = 10^{\text{SNR}_{\text{dB}}/10}$, where n is the channel dimension and h is the user channel. In each trial, $L = 6$ paths are generated with normalized angular variables $u, v \sim \mathcal{U}(-0.5, 0.5)$ and the propagation range r drawn uniformly from the near-field region $[r_F, r_R]$. These parameters are randomized across 500 trials to calculate the mean channel correlation. We compare the proposed LSE+R-SPARTA against three baselines: (i) *Exhaustive DFT Search*: A classical baseline that exhaustively probes all N DFT beams and selects the one with the highest received power (pilot overhead: N). (ii) *R-SPARTA* and (iii) *R-SWF*: Sparse phase retrieval solvers applied directly to the full DFT beamspace using Gaussian-masked sensing vectors. (iv) *LSE+R-SPARTA (Proposed)*: Our two-stage framework. Stage I performs structured exploration to identify a dominant beam subset ($T_1 = N$), and Stage II executes sparse PR on the resulting subspace ($M_2 = N$). Except for the exhaustive search, all PR-based methods utilize a total training overhead of $2N$.

The results are illustrated in Fig. 4. The proposed LSE+R-SPARTA achieves consistently high correlation across the entire SNR range, with performance improving monotonically from 0.693 at -15 dB to 0.957 at 15 dB. The performance gain is particularly prominent in the low-SNR regime, where direct sparse phase retrieval is highly susceptible to noise-induced ambiguities and suboptimal initializations. By performing adaptive subset selection in Stage I, we effectively improve the conditioning and local SNR of the subsequent recovery, leading to more reliable convergence. For instance,

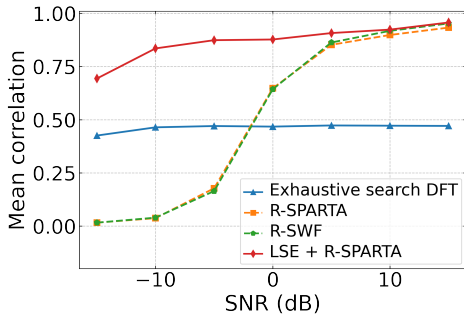


Fig. 4. Mean correlation versus SNR.

at -15 dB, our method yields a mean correlation of 0.693 compared to the 0.425 achieved by exhaustive DFT, reaching an absolute gain of 0.268. At 0 dB, our method reaches 0.877, whereas the non-adaptive R-SPARTA baseline only attains 0.648. At high SNR, our framework remains highly competitive, slightly outperforming R-SWF at 15 dB (0.957 vs. 0.952). These results validate that the proposed two-stage design significantly bolsters robustness without sacrificing high-SNR accuracy.

B. Ablation Study

To quantify the individual contributions of the key components within our two-stage framework, we perform an ablation study using the SNR sweep configuration described in Section V-A. We evaluate the performance of the proposed plus-kernel LSE+R-SPARTA against two modified variants, reporting the mean channel correlation at each SNR point as illustrated in Fig. 5.

Impact of Rician-Aware Recovery: We first isolate the significance of the statistical refinement by comparing our framework against a plus-kernel LSE+SPARTA variant. This version disables Stage I denoising and replaces the Rician-aware Stage II solver with a standard SPARTA algorithm. As shown in the results, removing the Rician awareness leads to a consistent degradation in correlation across the entire SNR spectrum. Specifically, at -15 dB, the mean correlation falls from 0.693 to 0.575, while at 15 dB, it decreases from 0.957 to 0.945. These findings confirm that integrating denoising and Rician-tailored recovery is critical for maintaining robust gains in practical non-coherent scenarios.

Impact of Physically-Motivated Kernel Design: We next examine the efficacy of the Stage I kernel by switching to a Laplace-kernel LSE+R-SPARTA variant. This setup retains the Rician-aware recovery pipeline but replaces the proposed cross-shaped kernel with a generic Laplace kernel. While this modification maintains competitive performance at high SNR (0.956 vs. 0.957 at 15 dB), it suffers significantly in low-SNR regimes, where the mean correlation drops from 0.693 to 0.565 at -15 dB. The superior robustness of the plus-shaped kernel at low SNR stems from its ability to accurately model the cross-shaped spatial reward map of the near-field DFT beamspace. By providing a more accurate inductive bias during the exploration phase, the plus kernel enables the BS to identify a more reliable beam support under heavy noise, thereby providing a better-conditioned subspace for the subsequent refinement stage.

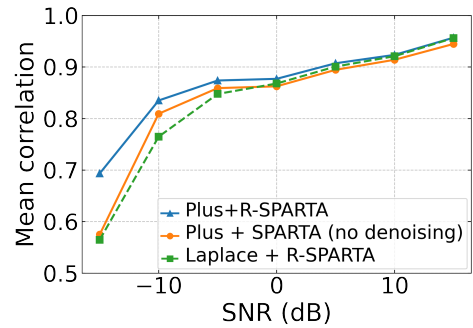


Fig. 5. Mean correlation versus SNR for ablated methods.

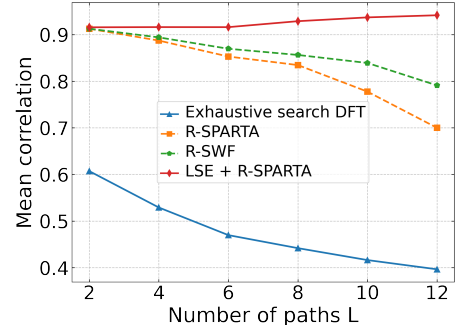


Fig. 6. Mean correlation versus number of path.

C. Impact of Number of Paths

We next evaluate the resilience of the proposed framework to varying channel sparsity by sweeping the number of propagation paths $L \in \{2, 4, 6, 8, 10, 12\}$. All other simulation parameters remain consistent with the setup in Section V-A. The resulting mean channel correlation ρ is illustrated in Fig. 6. As the multipath environment becomes increasingly complex (higher L), the baseline methods exhibit significant performance degradation. For the exhaustive DFT search, the mean correlation drops monotonically from 0.607 at $L = 2$ to 0.396 at $L = 12$. This sharp decline confirms that selecting a single best DFT beam is fundamentally inadequate for capturing the diverse spatial energy of a rich multipath environment. Similarly, the performance of R-SPARTA and R-SWF declines to 0.700 and 0.791 at $L = 12$, respectively. In contrast, LSE+R-SPARTA demonstrates remarkable stability, maintaining a correlation above 0.915 across all tested values of L . Notably, the performance even improves slightly as L increases, reaching 0.942 at $L = 12$. This translates to a relative improvement of approximately 34.5 % over R-SPARTA and 19.0 % over R-SWF in the most complex scenario ($L = 12$).

These results underscore the strength of our two-stage design: the structured exploration in Stage I adaptively identifies a beam subset that remains highly informative even as the multipath richness grows. By effectively "masking" the relevant subspace, the framework provides a stabilized environment for the subsequent Stage II recovery, whereas non-adaptive methods struggle to resolve the increased interference between paths.

D. Impact of User Distance and Near-Field Robustness

We next evaluate the resilience of the proposed framework to varying user-BS distances by sweeping the user range from

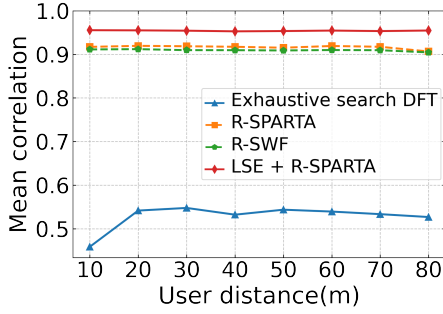


Fig. 7. Mean correlation versus user distance.

10 m to 80 m in increments of 10 m. For this experiment, the multipath complexity is fixed at $L = 4$ paths. At each distance point, we independently randomize the angles and scattering parameters for all paths, ensuring the user's primary range matches the prescribed grid value. The resulting mean channel correlation ρ is illustrated in Fig. 7. Across the entire evaluation range, LSE+R-SPARTA maintains a consistently high performance that is largely insensitive to distance variations, with the mean correlation stabilized near 0.95. In contrast, the R-SPARTA and R-SWF baselines achieve lower correlation values (approximately 0.91) and exhibit a slight performance degradation as the distance increases. The exhaustive DFT search remains the least effective baseline, showing significantly lower correlation and higher sensitivity to distance changes.

Specifically, at a close range of 10 m, LSE+R-SPARTA achieves a correlation of 0.955, outperforming R-SPARTA (0.917) by 4.2% and the exhaustive DFT search (0.459) by 108.3%. This superior performance persists even at a larger range of 80 m, where our method maintains a correlation of 0.955, exceeding R-SPARTA (0.907) by 5.3% and the exhaustive search (0.527) by 81.2%. These findings demonstrate that the structured exploration in Stage I effectively identifies a robust beam subset that captures the spherical wavefront characteristics reliably across a broad span of near-field distances.

VI. CONCLUSION

This paper proposed a two-stage framework for amplitude-only near-field beam training in multipath channels. Stage I performs GP-LSE-guided structured exploration on the standard 2D DFT grid using a physics-motivated cross-pattern-kernel that matches the near-field beamspace locality, enabling efficient discovery of dominant DFT support from debiased power feedback. Stage II then refines the channel over the learned subspace via Gaussian-masked sparse phase retrieval with a Rician-aware pseudo-amplitude denoising step, improving robustness under non-coherent measurements. Numerical results show that the proposed method consistently outperforms non-adaptive baselines, achieving a 35.3% relative improvement in channel correlation at moderate SNR, and remains stable across different multipath complexities and user distances. Overall, the proposed design offers a scalable and practical solution for near-field beam training when phase coherence cannot be guaranteed.

APPENDIX A

DERIVATION OF SPARSITY LEVEL FOR UPA

Under the separable lobe approximation, the number of active 2D DFT indices per path equals the occupied area divided by the grid cell size:

$$K_{\text{per-path}} \approx \frac{B_y(u, r) B_z(v, r)}{\Delta_y \Delta_z} = N_y N_z d^2 \frac{(1-u^2)(1-v^2)}{r^2 \Delta_y \Delta_z}. \quad (62)$$

For L disjoint paths, $\mathbb{E}[K_{\text{UPA}}] \approx L \mathbb{E}[K_{\text{per-path}}]$, which gives Eq. (18).

Because $u = \sqrt{1-v^2} s$ with $s = \sin \phi$, we compute

$$\begin{aligned} \mathbb{E}[(1-u^2)(1-v^2)] &= \mathbb{E}[(1-v^2)(1-(1-v^2)s^2)] \\ &= \mathbb{E}[1-v^2] - \mathbb{E}[(1-v^2)^2] \mathbb{E}[s^2], \end{aligned} \quad (63)$$

where we used the independence $v \perp s$. With $v \sim \mathcal{U}[v_1, v_2]$ and $s \sim \mathcal{U}[s_1, s_2]$,

$$\begin{aligned} \mathbb{E}[v^2] &= \frac{v_2^3 - v_1^3}{3(v_2 - v_1)} \triangleq \mu_2, \quad \mathbb{E}[v^4] = \frac{v_2^5 - v_1^5}{5(v_2 - v_1)} \triangleq \mu_4, \\ \mathbb{E}[s^2] &= \frac{s_2^3 - s_1^3}{3(s_2 - s_1)} \triangleq \nu_2, \end{aligned} \quad (64)$$

and

$$\mathbb{E}[1-v^2] = 1 - \mu_2, \quad \mathbb{E}[(1-v^2)^2] = 1 - 2\mu_2 + \mu_4,$$

which yields Eq. (22). Finally, since $r \sim \mathcal{U}[r_1, r_2]$,

$$\mathbb{E}\left[\frac{1}{r^2}\right] = \frac{1}{r_2 - r_1} \int_{r_1}^{r_2} \frac{1}{r^2} dr = \frac{1}{r_2 - r_1} \left(\frac{1}{r_1} - \frac{1}{r_2}\right),$$

which gives Eq. (21). Substituting these into Eq. (18) yields Eq. (20).

APPENDIX B

UNBIASEDNESS AND NOISE STATISTICS OF STAGE I POWER FEEDBACK

Let $y_t = s_t + w_t$ with $s_t \triangleq \mathbf{h}^H \mathbf{v}_{i_t} x_t$ and $w_t \sim \mathcal{CN}(0, \sigma^2)$. Expanding the squared magnitude yields

$$|y_t|^2 = |s_t|^2 + |w_t|^2 + 2\Re\{s_t^* w_t\}. \quad (65)$$

Therefore, conditioning on \mathbf{h} (equivalently on s_t) gives

$$\mathbb{E}[|y_t|^2 | \mathbf{h}] = |s_t|^2 + \mathbb{E}[|w_t|^2] = f(i_t) + \sigma^2, \quad (66)$$

which justifies $\tilde{z}_t = |y_t|^2 - \sigma^2$ as a conditionally unbiased estimate of $f(i_t)$. The centered residual admits the decomposition

$$\tilde{\varepsilon}_t = \tilde{z}_t - f(i_t) = (|w_t|^2 - \sigma^2) + 2\Re\{s_t^* w_t\}. \quad (67)$$

For $w_t \sim \mathcal{CN}(0, \sigma^2)$, $|w_t|^2$ follows an exponential distribution with mean σ^2 and variance σ^4 , hence $(|w_t|^2 - \sigma^2)$ is sub-exponential (light-tailed). Moreover, $2\Re\{s_t^* w_t\}$ is real Gaussian with zero mean and variance $2\sigma^2 |s_t|^2 = 2\sigma^2 f(i_t)$. Consequently, the conditional variance of the power feedback is

$$\text{Var}(|y_t|^2 | \mathbf{h}) = \sigma^4 + 2\sigma^2 f(i_t), \quad (68)$$

which is heteroscedastic across probed beams.

We further assume that the beamspace power map is uniformly bounded,

$$0 \leq f(i) \leq f_{\max}, \quad \forall i \in \mathcal{I}, \quad (69)$$

where f_{\max} is a finite constant induced by practical transmit-power and array-gain limits. Under Eq. (69), Eq. (68) implies the uniform variance bound

$$\text{Var}(\tilde{\varepsilon}_t | \mathbf{h}) = \sigma^4 + 2\sigma^2 f(i_t) \leq \sigma^4 + 2\sigma^2 f_{\max}. \quad (70)$$

The residual $\tilde{\varepsilon}_t$ in Eq. (67) is a sum of a centered exponential term and a Gaussian term, hence it is conditionally sub-exponential. In particular, there exist absolute constants $c_0, c_1 > 0$ such that for all $u \geq 0$,

$$\Pr(|\tilde{\varepsilon}_t| \geq u | \mathbf{h}) \leq 2 \exp\left(-c_0 \min\left\{\frac{u^2}{\sigma^4 + 2\sigma^2 f_{\max}}, \frac{u}{\sigma^2}\right\}\right). \quad (71)$$

We next use the sub-exponential tail bound Eq. (71) to construct a high-probability bounded-noise event over a finite Stage I budget T_1 . This event is only an analysis device; the implementation always uses the original debiased feedback \tilde{z}_t .

Fix $\delta_{\text{bd}} \in (0, 1)$ and define, for $t = 1, \dots, T_1$, the deterministic threshold

$$B_t \triangleq c_1 \left(\sigma^2 \log\left(\frac{\pi^2 t^2}{12\delta_{\text{bd}}}\right) + \sqrt{(\sigma^4 + 2\sigma^2 f_{\max}) \log\left(\frac{\pi^2 t^2}{12\delta_{\text{bd}}}\right)} \right), \quad (72)$$

where $c_1 > 0$ is an absolute constant as in Eq. (71). Define the event

$$\mathcal{E}_{\text{bd}}(T_1) \triangleq \bigcap_{t=1}^{T_1} \{|\tilde{\varepsilon}_t| \leq B_t\}. \quad (73)$$

By Eq. (71) and a union bound over $t = 1, \dots, T_1$, the choice Eq. (72) ensures

$$\Pr(\mathcal{E}_{\text{bd}}(T_1)) \geq 1 - \delta_{\text{bd}}. \quad (74)$$

On $\mathcal{E}_{\text{bd}}(T_1)$, the Stage I feedback obeys

$$\tilde{z}_t = f(i_t) + \tilde{\varepsilon}_t, \quad |\tilde{\varepsilon}_t| \leq B_t \leq B_{T_1}, \quad t = 1, \dots, T_1. \quad (75)$$

Since bounded random variables are sub-Gaussian, Hoeffding's lemma implies that on $\mathcal{E}_{\text{bd}}(T_1)$ the noise $\tilde{\varepsilon}_t$ is conditionally sub-Gaussian with a conservative variance proxy on the order of $B_{T_1}^2$. Accordingly, in the GP posterior update Eq. (31) we may use an effective parameter $\sigma_\varepsilon^2 \gtrsim B_{T_1}^2$ for analysis.

APPENDIX C GP-LSE GUARANTEE

We provide a self-contained proof sketch of the standard GP-LSE guarantee on the finite domain \mathcal{I} . Throughout, $(\mu_{t-1}(\cdot), \sigma_{t-1}(\cdot))$ denote the GP posterior mean and standard deviation computed via kernel ridge regression with regularization σ_ε^2 in Eq. (31). All results are stated on the bounded-noise event $\mathcal{E}_{\text{bd}}(T_1)$ in Eq. (73), under which $\tilde{z}_t = f(i_t) + \tilde{\varepsilon}_t$ and $|\tilde{\varepsilon}_t| \leq B_{T_1}$ for all $t \leq T_1$ and thus the noise is sub-Gaussian.

A. Uniform confidence event

We work on the bounded-noise event $\mathcal{E}_{\text{bd}}(T_1)$ constructed in Appendix B. On $\mathcal{E}_{\text{bd}}(T_1)$, the debiased feedback obeys

$$\tilde{z}_t = f(i_t) + \tilde{\varepsilon}_t, \quad \mathbb{E}[\tilde{\varepsilon}_t | \mathcal{F}_{t-1}] = 0, \quad |\tilde{\varepsilon}_t| \leq B_t, \quad \forall t \leq T_1, \quad (76)$$

where $\{\mathcal{F}_t\}$ is the natural filtration and $\{B_t\}$ is defined in Eq. (72). Since $\{B_t\}$ is nondecreasing by construction, it follows that $|\tilde{\varepsilon}_t| \leq B_{T_1}$ for all $t \leq T_1$.

We further assume the standard RKHS complexity condition used by kernelized bandit analyses: the unknown power map f is a fixed function in \mathcal{H}_k with $\|f\|_{\mathcal{H}_k} \leq B_f$. This is an agnostic function-class condition: it requires that f be regular under k . Because our cross-pattern kernel Eq. (28) encodes the near-field DFT-beam locality observed in Fig. 2-Fig. 3, it is reasonable that the induced RKHS complexity of f is moderate.

Recall the GP confidence interval in the main text:

$$Q_t(i) \triangleq \left[\mu_{t-1}(i) - \sqrt{\beta_t} \sigma_{t-1}(i), \mu_{t-1}(i) + \sqrt{\beta_t} \sigma_{t-1}(i) \right], \quad (77)$$

which matches Eq. (35). The shrinking interval used by GP-LSE is defined as

$$C_t(i) \triangleq \bigcap_{s=1}^t Q_s(i), \quad \ell_t(i) = \min C_t(i), \quad u_t(i) = \max C_t(i). \quad (78)$$

Lemma 1. Fix $\delta \in (0, 1)$. Choose a nondecreasing exploration sequence

$$\beta_t = 2B_f^2 + 300\gamma_{t-1} \log^3\left(\frac{t}{\delta}\right), \quad t \geq 1, \quad (79)$$

where γ_t is the maximum information gain of kernel k on \mathcal{I} under noise parameter σ_ε^2 . Then, conditioned on $\mathcal{E}_{\text{bd}}(T_1)$, with probability at least $1 - \delta$, for all $t \geq 1$ and all $i \in \mathcal{I}$,

$$|f(i) - \mu_{t-1}(i)| \leq \sqrt{\beta_t} \sigma_{t-1}(i). \quad (80)$$

Consequently, $f(i) \in Q_t(i)$ for all i, t , and thus $f(i) \in C_t(i)$ for all i, t .

Proof. On $\mathcal{E}_{\text{bd}}(T_1)$, the observation noise $\tilde{\varepsilon}_t$ in Eq. (76) is a uniformly bounded martingale difference sequence over $t \leq T_1$. Therefore, the RKHS-based GP bandit confidence analysis applies. In particular, the escape-event argument and the martingale concentration step in Theorem 6 of [27] imply that the posterior deviation is uniformly controlled by $\sqrt{\beta_t} \sigma_{t-1}(i)$ when β_t is chosen as in Eq. (79). This yields Eq. (80). The last inclusion follows from the definitions Eq. (77)-Eq. (78). \square

Define the overall ‘‘good’’ event as

$$\mathcal{E} \triangleq \mathcal{E}_{\text{bd}}(T_1) \cap \mathcal{E}_{\text{ci}}, \quad (81)$$

where \mathcal{E}_{ci} denotes the uniform confidence event in Eq. (80). Since $\Pr(\mathcal{E}_{\text{bd}}(T_1)) \geq 1 - \delta_{\text{bd}}$ and $\Pr(\mathcal{E}_{\text{ci}} | \mathcal{E}_{\text{bd}}(T_1)) \geq 1 - \delta$,

$$\begin{aligned} \Pr(\mathcal{E}) &= \Pr(\mathcal{E}_{\text{bd}}(T_1) \cap \mathcal{E}_{\text{ci}}) \\ &= \Pr(\mathcal{E}_{\text{bd}}(T_1)) \Pr(\mathcal{E}_{\text{ci}} | \mathcal{E}_{\text{bd}}(T_1)) \\ &\geq (1 - \delta_{\text{bd}})(1 - \delta) \geq 1 - (\delta_{\text{bd}} + \delta). \end{aligned} \quad (82)$$

B. Correctness of the level-set estimate

We now prove the ϵ -accurate inclusion property under the event \mathcal{E} in Eq. (81). Recall the classification rule in Eq. (39)-Eq. (41) and the fact $f(i) \in C_T(i)$ from Lemma 1.

a) *Upper inclusion.*

Fix any $i \in \mathcal{H}_T$. By the classification rule Eq. (39) we have $\ell_T(i) > \tau - \epsilon$. On the event \mathcal{E} , Lemma 1 gives $f(i) \in C_T(i)$, hence $f(i) \geq \min C_T(i) = \ell_T(i)$. Combining the two inequalities yields $f(i) > \tau - \epsilon$, i.e., $i \in \{j \in \mathcal{I} : f(j) \geq \tau - \epsilon\}$. Since $i \in \mathcal{H}_T$ was arbitrary, we conclude

$$\mathcal{H}_T \subseteq \{i \in \mathcal{I} : f(i) \geq \tau - \epsilon\}. \quad (83)$$

b) *Lower inclusion.*

Let i satisfy $f(i) \geq \tau + \epsilon$. On \mathcal{E} , Lemma 1 implies $f(i) \in C_t(i)$ for all t . In particular, $u_t(i) \geq f(i) \geq \tau + \epsilon$ for all t , so i can never satisfy the (lower) classification condition for \mathcal{L}_t in Eq. (40). Hence i is never permanently placed into \mathcal{L}_t . When the algorithm terminates, it enforces $\mathcal{U}_T = \emptyset$, so every index is classified into either \mathcal{H}_T or \mathcal{L}_T . Therefore such i must belong to \mathcal{H}_T , i.e.,

$$\{i : f(i) \geq \tau + \epsilon\} \subseteq \mathcal{H}_T. \quad (84)$$

Combining Eq. (83) and Eq. (84) gives the desired ϵ -accurate level-set guarantee.

C. *Sample complexity via information gain*

We bound the number of GP-LSE queries until termination. The key link is that GP posterior variances accumulate at most on the order of the kernel information gain; this is standard in GP-LSE analyses [27], [30].

Recall $Q_t(i)$ in Eq. (77) and $C_t(i) = \cap_{s \leq t} Q_s(i)$ in Eq. (78). Since $C_t(i) \subseteq Q_t(i)$, its width is no larger than that of $Q_t(i)$. Thus, for any $i \in \mathcal{U}_t$,

$$\begin{aligned} a_t(i) &\leq \frac{1}{2}(u_t(i) - \ell_t(i)) \\ &\leq \frac{1}{2}(\max Q_t(i) - \min Q_t(i)) \\ &= \sqrt{\beta_t} \sigma_{t-1}(i). \end{aligned} \quad (85)$$

Lemma 2. *Let $\{i_s\}_{s=1}^t$ be the queried sequence and let $\sigma_{s-1}^2(i_s)$ be the GP posterior variance computed with regularization σ_ϵ^2 as in Eq. (31). Then (refer equation; sample complexity)*

$$\log \det(\mathbf{I}_t + \sigma_\epsilon^{-2} \mathbf{K}_t) = \sum_{s=1}^t \log(1 + \sigma_\epsilon^{-2} \sigma_{s-1}^2(i_s)), \quad (86)$$

where \mathbf{K}_t is kernel matrix defined in Section IV-A. Consequently,

$$\sum_{s=1}^t \sigma_{s-1}^2(i_s) \leq \frac{2}{\log(1 + \sigma_\epsilon^{-2})} \gamma_t \triangleq C_1 \gamma_t, \quad (87)$$

where γ_t is defined in Eq. (37) and $C_1 > 0$ depends only on σ_ϵ^2 .

Proof. The details can be found in [27] and [30] and here we provide a proof sketch. The identity Eq. (86) is the standard incremental log-determinant decomposition for GP posteriors. Since $\sigma_{s-1}^2(i_s) \in [0, k(i_s, i_s)]$ and $k(i, i) \leq 1$, concavity of $\log(1 + \sigma_\epsilon^{-2} x)$ on $x \in [0, 1]$ yields $\log(1 + \sigma_\epsilon^{-2} x) \geq x \log(1 + \sigma_\epsilon^{-2})$. Summing this inequality over s and combining with Eq. (86) gives $\sum_{s=1}^t \sigma_{s-1}^2(i_s) \leq \log \det(\mathbf{I}_t + \sigma_\epsilon^{-2} \mathbf{K}_t) / \log(1 + \sigma_\epsilon^{-2})$. Finally, by definition of γ_t in Eq. (37), $\log \det(\mathbf{I}_t + \sigma_\epsilon^{-2} \mathbf{K}_t) \leq 2\gamma_t$. \square

Let $m_t \triangleq \max_{i \in \mathcal{U}_{t-1}} a_t(i)$. By the GP-LSE selection rule Eq. (43), $m_t = a_t(i_t)$. Moreover, $\{m_t\}$ is non-increasing because confidence sets shrink and the undecided set only shrinks [30]. Hence $t m_t^2 \leq \sum_{s=1}^t m_s^2 = \sum_{s=1}^t a_s^2(i_s)$.

Using Eq. (85) and monotonicity of $\{\beta_t\}$,

$$\sum_{s=1}^t a_s^2(i_s) \leq \sum_{s=1}^t \beta_s \sigma_{s-1}^2(i_s) \leq \beta_t \sum_{s=1}^t \sigma_{s-1}^2(i_s) \leq C_1 \beta_t \gamma_t, \quad (88)$$

where the last step uses Lemma 2. Therefore,

$$m_t \leq \sqrt{\frac{C_1 \beta_t \gamma_t}{t}}. \quad (89)$$

A sufficient condition for the stopping criterion $m_t \leq \epsilon$ is

$$t \geq \frac{C_1 \beta_t \gamma_t}{\epsilon^2}. \quad (90)$$

With β_t chosen as in Theorem 6 of [27], i.e., Eq. (79), we obtain the stated Stage I sample complexity

$$T_1 = \tilde{\mathcal{O}}\left(\frac{\beta_{T_1} \gamma_{T_1}}{\epsilon^2}\right) = \tilde{\mathcal{O}}\left(\frac{B_f^2 \gamma_{T_1} + \gamma_{T_1}^2}{\epsilon^2}\right). \quad (91)$$

APPENDIX D

STATISTICAL RATIONALE OF THE RICIAN DENOISING IN STAGE II

This appendix explains why the Stage II pseudo-amplitude $\tilde{\psi}_p = \sqrt{[y_p^2 - \sigma^2]_+}$ in Eq. (53) can be interpreted as a noisy observation of the noiseless amplitude, thereby connecting Stage II to the standard noisy-amplitude sparse phase retrieval formulation [24].

In Stage II, the low-dimensional magnitude measurement is $y_p = |\mathbf{g}_p^H \mathbf{s}_{\mathcal{S}} + w_p|$ with $w_p \sim \mathcal{CN}(0, \sigma^2)$. Let

$$a_p \triangleq |\mathbf{g}_p^H \mathbf{s}_{\mathcal{S}}| \quad (92)$$

denote the noiseless amplitude. Consider the debiased intensity

$$\tilde{z}_p \triangleq y_p^2 - \sigma^2. \quad (93)$$

Using the same decomposition as in Appendix B (with $s \leftarrow a_p e^{j\varphi_p}$), we obtain the conditional unbiasedness

$$\tilde{z}_p = a_p^2 + \varepsilon_p, \quad \mathbb{E}[\varepsilon_p | \mathbf{g}_p] = 0, \quad (94)$$

and the conditional variance

$$\text{Var}(\varepsilon_p | \mathbf{g}_p) = \sigma^4 + 2\sigma^2 a_p^2. \quad (95)$$

Hence, \tilde{z}_p is a zero-mean-fluctuated observation of a_p^2 with heteroscedastic variability.

Stage II applies a nonnegativity projection and square-root mapping:

$$\tilde{\psi}_p = \sqrt{[y_p^2 - \sigma^2]_+} = \sqrt{[a_p^2 + \varepsilon_p]_+}. \quad (96)$$

When the SNR is moderate-to-high so that a_p is not too small for most p , we can relate $\tilde{\psi}_p$ to a_p through a deterministic bound. Specifically, on the event $a_p^2 + \varepsilon_p \geq 0$ (which is always enforced by $[\cdot]_+$), by the mean value theorem applied to $\sqrt{\cdot}$, we have

$$|\tilde{\psi}_p - a_p| = \left| \sqrt{[a_p^2 + \varepsilon_p]_+} - \sqrt{a_p^2} \right| \leq \frac{|\varepsilon_p|}{\sqrt{[a_p^2 + \varepsilon_p]_+} + a_p}. \quad (97)$$

In particular, whenever $|\varepsilon_p| \leq a_p^2/2$ (hence $[a_p^2 + \varepsilon_p]_+ \geq a_p^2/2$), the denominator in Eq. (97) is lower bounded as $\sqrt{[a_p^2 + \varepsilon_p]_+} + a_p \geq (1 + 1/\sqrt{2})a_p$, yielding

$$|\tilde{\psi}_p - a_p| \leq \frac{|\varepsilon_p|}{(1 + 1/\sqrt{2})a_p} \leq \frac{|\varepsilon_p|}{a_p}. \quad (98)$$

Such a condition is mild for measurements probing dominant-support beams discovered in Stage I, since the corresponding a_p is typically above the noise floor for a large fraction of p . Therefore, $\tilde{\psi}_p$ can be interpreted as a noisy amplitude observation of a_p , where the effective disturbance is induced by the Rician fluctuation ε_p and the square-root mapping.

From Eq. (96)-Eq. (97), whenever $[a_p^2 + \varepsilon_p]_+ > 0$, the mapping $\tilde{\psi}_p = \sqrt{[a_p^2 + \varepsilon_p]_+}$ induces an additive amplitude-noise model $\tilde{\psi}_p = a_p + \eta_p$ with a bounded perturbation controlled by the bound in Eq. (97). Hence, conditioned on the event $[a_p^2 + \varepsilon_p]_+ > 0$, the Stage II data fit exactly the “noisy amplitude” setting under which SPARTA is empirically robust [24]. On the other hand, when $a_p^2 + \varepsilon_p \leq 0$, the projection in Eq. (96) clips the pseudo-amplitude to $\tilde{\psi}_p = 0$, which corresponds to below-noise-floor samples; these are naturally suppressed by SPARTA’s truncation and hard-thresholding mechanism. Therefore, in the moderate-to-high SNR regime, which is typical for received signal of dominant DFT code-words, the proposed amplitude construction is compatible with SPARTA and leads to accurate refinement in practice.

REFERENCES

- [1] P. Testolina, M. Polese, and T. Melodia, “Sharing spectrum and services in the 7-24 GHz upper midband,” *IEEE Communications Magazine*, vol. 62, no. 8, pp. 170–177, Aug. 2024.
- [2] J. M. Jornet, N. Yang, R. Nichols, S. Nie, C. Huang, and R. K. Mallik, “Terahertz communications and sensing for 6g and beyond: How far are we?” *IEEE Wireless Commun.*, vol. 31, no. 1, pp. 8–9, Feb. 2024.
- [3] I. F. Akyildiz, C. Han, Z. Hu, S. Nie, and J. M. Jornet, “Terahertz band communication: An old problem revisited and research directions for the next decade,” *IEEE Trans. Commun.*, vol. 70, no. 6, pp. 4250–4285, Jun. 2022.
- [4] S. Kang, G. Geraci, M. Mezzavilla, and S. Rangan, “Cellular wireless networks in the upper mid-band,” *IEEE Open Journal of the Communications Society*, vol. 5, pp. 2058–2075, 2024.
- [5] M. Zhang et al., “New mid-band for 6G: Several considerations from the channel propagation characteristics perspective,” *IEEE Communications Magazine*, vol. 63, no. 1, pp. 175–180, Jan. 2025.
- [6] H. Lu et al., “A tutorial on near-field xl-mimo communications towards 6G,” *IEEE Communications Surveys & Tutorials*, vol. 26, no. 4, pp. 2213–2257, 2024.
- [7] A. Rasteh, R. P. Hari, H. Guo, M. Mezzavilla, and S. Rangan, “Near-field measurement system for the upper mid-band,” in *2024 58th Asilomar Conference on Signals, Systems, and Computers*, 2024, pp. 1684–1689.
- [8] Y. Liu, Z. Wang, J. Xu, C. Ouyang, X. Mu, and R. Schober, “Near-field communications: A tutorial review,” *IEEE Open J. Commun. Soc.*, vol. 4, pp. 1999–2049, Aug. 2023.
- [9] M. Cui and L. Dai, “Channel estimation for extremely large-scale mimo: Far-field or near-field?” *IEEE Trans. Commun.*, vol. 70, no. 4, pp. 2663–2677, Apr. 2022.
- [10] T. Zheng, M. Cui, Z. Wu, and L. Dai, “Near-field wideband beam training based on distance-dependent beam split,” *IEEE Trans. Wireless Commun.*, vol. 24, no. 2, pp. 1278–1292, Feb. 2025.
- [11] H. Wang, J. Fang, H. Duan, and H. Li, “Fast hybrid far/near-field beam training for extremely large-scale millimeter wave/terahertz systems,” *IEEE Trans. Commun.*, pp. 1–1, 2024.
- [12] X. Shi, J. Wang, Z. Sun, and J. Song, “Spatial-chirp codebook-based hierarchical beam training for extremely large-scale massive mimo,” *IEEE Trans. Wireless Commun.*, vol. 23, no. 4, pp. 2824–2838, Apr. 2024.
- [13] Y. Chen, C. Han, and E. Björnson, “Can far-field beam training be deployed for cross-field beam alignment in terahertz um-mimo communications?” *IEEE Transactions on Wireless Communications*, vol. 23, no. 10, pp. 14 972–14 987, Oct. 2024.
- [14] X. Zhang, W. Chen, W. Zheng, Z. Xia, and Y. Wang, “Localization of near-field sources: A reduced-dimension music algorithm,” *IEEE Communications Letters*, vol. 22, no. 7, pp. 1422–1425, 2018.
- [15] X. Yuan, M. Zhang, Y. Zheng, B. Teng, and W. Jiang, “Scalable near-field localization based on partitioned large-scale antenna array,” *IEEE Trans. Wireless Commun.*, pp. 1–1, Jan. 2024.
- [16] J. Lee, G.-T. Gil, and Y. H. Lee, “Channel estimation via orthogonal matching pursuit for hybrid mimo systems in millimeter wave communications,” *IEEE Transactions on Communications*, vol. 64, no. 6, pp. 2370–2386, Jun. 2016.
- [17] R. Méndez-Rial, C. Rusu, N. González-Prelcic, A. Alkhateeb, and J. Heath Robert W., “Hybrid MIMO architectures for millimeter wave communications: Phase shifters or switches?” *IEEE Access*, vol. 4, pp. 247–267, 2016.
- [18] Z. Wang et al., “Sparsity-aware near-field beam training via multi-beam combination,” *Accepted by IEEE Globecom 2025, arXiv preprint arXiv:2505.08267*, 2025. arXiv: 2505.08267 [eess.SP]. [Online]. Available: <https://arxiv.org/abs/2505.08267>
- [19] C. Hu, X. Wang, L. Dai, and J. Ma, “Partially coherent compressive phase retrieval for millimeter-wave massive MIMO channel estimation,” *IEEE Transactions on Signal Processing*, vol. 68, pp. 1673–1687, 2020.
- [20] J. Chen, F. Gao, M. Jian, and W. Yuan, “Hierarchical codebook design for near-field mmwave mimo communications systems,” *IEEE Wireless Commun. Lett.*, vol. 12, no. 11, pp. 1926–1930, Nov. 2023.
- [21] E. J. Candès, X. Li, and M. Soltanolkotabi, “Phase retrieval via wirtinger flow: Theory and algorithms,” *IEEE Transactions on Information Theory*, vol. 61, no. 4, pp. 1985–2007, 2015.
- [22] G. Wang, G. B. Giannakis, and Y. Chen, “Solving systems of random quadratic equations via truncated amplitude flow,” *IEEE Transactions on Information Theory*, vol. 64, no. 2, pp. 773–794, 2018.
- [23] Z. Yuan, H. Wang, and Q. Wang, “Phase retrieval via Sparse Wirtinger Flow,” *Journal of Computational and Applied Mathematics*, vol. 355, pp. 162–173, Aug. 2019, ISSN: 03770427.
- [24] G. Wang, L. Zhang, G. B. Giannakis, M. Akcakaya, and J. Chen, “Sparse phase retrieval via truncated amplitude flow,” *IEEE Transactions on Signal Processing*, vol. 66, no. 2, pp. 479–491, 2018.
- [25] X. Li, J. Fang, H. Duan, Z. Chen, and H. Li, “Fast beam alignment for millimeter wave communications: A sparse encoding and phaseless decoding approach,” *IEEE Transactions on Signal Processing*, vol. 67, no. 17, pp. 4402–4417, Sep. 2019.
- [26] T. Qiu, X. Fu, N. D. Sidiropoulos, and D. P. Palomar, “Miso channel estimation and tracking from received signal strength feedback,” *IEEE Transactions on Signal Processing*, vol. 66, no. 7, pp. 1691–1704, 2018.
- [27] N. Srinivas, A. Krause, S. M. Kakade, and M. W. Seeger, “Gaussian process optimization in the bandit setting: No regret and experimental design,” in *Proceedings of the 27th International Conference on Machine Learning (ICML-10)*, Omnipress, pp. 1015–1022.
- [28] Z. Wu and L. Dai, “Multiple Access for Near-Field Communications: SDMA or LDMA?” *IEEE Journal on Selected Areas in Communications*, vol. 41, no. 6, pp. 1918–1935, Jun. 2023, ISSN: 0733-8716, 1558-0008.
- [29] Z. Wang, R. Kiran, S. Tsai, and R. Zhang, *Low-complexity near-field beam training with dft codebook based on beam pattern analysis*, Mar. 2025. Accepted by IEEE Globecom 2025, arXiv: 2503.21954 (eess.SP).
- [30] A. Gotovos, N. Casati, G. Hitz, and A. Krause, “Active learning for level set estimation,” in *Proceedings of the Twenty-Third International Joint Conference on Artificial Intelligence (IJCAI)*, 2013.
- [31] N. Srinivas, A. Krause, S. M. Kakade, and M. W. Seeger, “Information-theoretic regret bounds for gaussian process optimization in the bandit setting,” *IEEE Transactions on Information Theory*, vol. 58, no. 5, pp. 3250–3265, 2012.